

A Photothermal Spectrometer for Fast and Background-Free Detection of Individual Nanoparticles in Flow

Richard Maceiczky,[†] Hisashi Shimizu,[§] David Müller,^{†,‡,Ⓢ} Takehiko Kitamori,[§] and Andrew deMello^{*,†,Ⓢ}

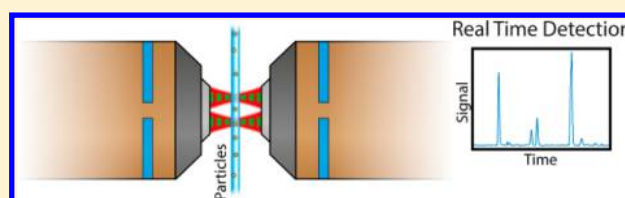
[†]Institute for Chemical and Bioengineering, Department of Chemistry and Applied Biosciences, ETH Zürich, Vladimir-Prelog-Weg 1, 8093 Zürich, Switzerland

[‡]Centre Suisse d'Electronique et de Microtechnique (CSEM), Bahnhofstrasse 1, 7302 Landquart, Switzerland

[§]Department of Applied Chemistry, School of Engineering, The University of Tokyo, 7-3-1, Hongo, Bunkyo-ku, Tokyo 113-8656, Japan

Supporting Information

ABSTRACT: Sensitive detection and quantification of individual plasmonic nanoparticles is critical in a range of applications in the biological, nanomaterials, and analytical sciences. Although a wide range of techniques can be applied to the analysis of immobilized particles, high-throughput analysis of nanoscale species in flow is surprisingly underdeveloped. To address this shortcoming, we present an ultrasensitive, background-free technique based on the photothermal effect and termed differential detection photothermal interferometry (DDPI). We show, both theoretically and experimentally, that DDPI can specifically extract either the phase or amplitude of a photothermal signal. We then quantitatively detect 10 and 20 nm diameter gold nanoparticles at femtomolar concentrations and at linear flow speeds of 10 mm/s. In the case of 50 nm gold particles, we operate at an even higher linear flow speed of 100 mm/s, corresponding to an analyzed volume of more than 1 nL/s. This allows quantification of particle content at attomolar to femtomolar concentrations and counting rates between 0.1 and 400 particles per second. Finally, we confirm that the signal follows the size-dependent variations predicted by Mie theory.



Because of their large absorbance and scattering cross sections, plasmonic nanoparticles are of considerable scientific and commercial interest for a wide range of applications such as in vitro diagnostics,¹ sensing,² photothermal therapy,³ and biological assays.^{4,5} Consequently, the demand for detection techniques able to sensitively detect, identify, and quantify at the single particle level is high.⁶ In this respect, a range of single nanoparticle sensing methods based on scattering have been reported, including interferometry,^{7,8} particle tracking in nanofluidic fibers,⁹ photoacoustic spectroscopy,¹⁰ flow cytometry,¹¹ evanescent wave induced scattering,¹² photonic nanojets,¹³ and correlation spectroscopy.^{14,15} Despite such developments, detection of nanoparticle absorbance, as opposed to scattering, is potentially more sensitive because the absorbance cross section shows a significantly weaker dependence on size than the scattering cross section.¹⁶ Photothermal spectroscopies take advantage of this feature and have proved to be extremely sensitive in the detection of individual gold nanoparticles immobilized on surfaces,¹⁷ within living cells,^{18,19} as well as in flow.^{20–22} However, most if not all of the above listed methods are unsuited for use in quantitative analysis (typically in the fL-regime) and long integration times (on the order of a few milliseconds).²³ Many of these methods also require elaborate structures to interface the detection setup with the analyte flow (such as nanochannels⁷ or sheath flows¹²) or rely on surface-immobilization of the particles. All of these

issues hamper the facile and direct integration of single nanoparticle detectors with microfluidic systems. This is especially important, since microfluidic systems provide for enhanced heat and mass transfer as well as exquisite control of reaction conditions, and have been shown to provide unique and highly efficient environments in which to synthesize and analyze a wide variety of nanomaterials.^{24–28} To mitigate such issues, we herein describe a novel and high-throughput photothermal detection technique named Differential Detection Photothermal Interferometry (DDPI) which enables direct, rapid and accurate nanoparticle characterization down to attomolar concentrations. Furthermore, facile integration of DDPI with microfluidic systems allows for ultrafast and ultrasensitive analysis of nonfluorescent nanoparticles in flow.

Although single-beam photothermal detection of gold nanoparticles has recently been reported,²⁹ a pump–probe configuration is intrinsically superior to a single-beam format due to higher signal-to-noise ratios and inherent insensitivity to nonabsorbing scatterers.³⁰ In a pump–probe photothermal configuration, a focused, amplitude-modulated excitation laser at a wavelength close to the plasmon resonance is used to excite a gold nanoparticle, which in turn will release heat into the surrounding medium. The released heat modifies the local

Received: November 17, 2016

Accepted: January 12, 2017

Published: January 12, 2017

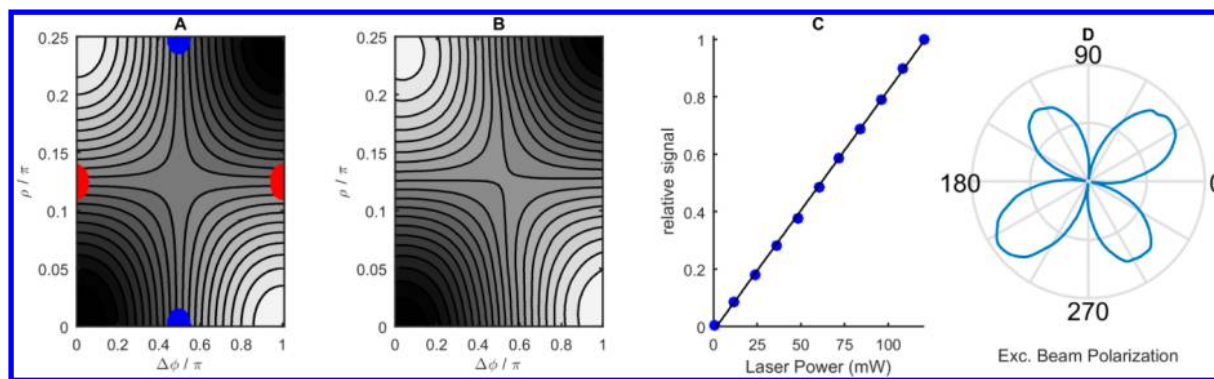


Figure 1. Theoretical (A) and experimental (B) dependence of the normalized light intensity received by one photodiode on the phase shift introduced by the second Wollaston prism ($\Delta\phi$) and on the half-wave-plate rotation (ρ). The red areas indicate the amplitude-sensitive mode, whereas the blue areas indicate the phase-sensitive mode. (C) Normalized photothermal signal as a function of excitation laser power (measured using 100 μ M Sunset Yellow in water and a single-beam configuration). (D) Normalized photothermal signal as a function of excitation laser polarization (measured with 100 μ M Sunset Yellow in water). Minima correspond to an equal distribution of the excitation laser in the two arms, with maxima corresponding to the excitation beam being directed only into one arm. As expected, four maxima and four minima with a separation of 90° are present.

refractive index around the particle in a periodic fashion and in turn induces a thermal lens oscillating with a defined modulation frequency. A collinear, nonresonant probe beam can be diffracted by this thermal lens, thereby experiencing a periodic phase and amplitude change that can be detected in the far field directly or interferometrically using a lock-in amplifier.³¹ Interferometric detection is highly sensitive and suppresses noise independent of frequency. However, response to a phase or amplitude change for complete destructive interference (where noise is minimal) is small, nonlinear and invariably carries any noise present in the system because the signal corresponds to a deviation from complete interference and is therefore subjected to the same relative amplitude noise as the incoming beam. Furthermore, depolarization of the beams by optical components negatively affects recombination and thus noise suppression.³² To address these issues, we propose DDPI as a measurement scheme that generates the signal interferometrically while eliminating noise at all frequencies via differential detection. Such an approach allows noise suppression to be decoupled from the efficiency of beam recombination, and it specifically accesses the phase or amplitude component of the photothermal signal at extremely low noise levels, while maintaining linearity in the response of the interferometer.

To generate the two arms of the interferometer, we use a Wollaston prism to separate the superimposed probe and excitation beams (modulated at 100 kHz) into two beams of equal intensity and perpendicular polarization. A 4f-system couples the light into a microscope objective which focuses the beams at the center of a fused silica capillary, resulting in a lateral focal spot separation of approximately 40 μ m. An identical objective and 4f-system then collects light exiting the capillary before a second Wollaston prism recombines the two arms. A spectral filter removes the excitation light, and the probe beam passes through a half wave plate. Subsequently, a polarizing beam splitter separates the probe beam into its two polarization components and projects each onto an amplified silicon photodiode. The photodiodes connect to the differential input of a lock-in amplifier, which recovers the oscillating component of the signal. Lateral translation of the second Wollaston prism along with rotation of the half-wave plate sets

the working point of the interferometer. A full schematic of the optical setup is provided in Figure S1.

The theoretical and experimental light intensities received by the photodiodes (which depend on the phase shift between the beams introduced by the Wollaston prism and on the polarization rotation produced by the half wave plate) are in excellent agreement, as shown in Figure 1A,B.

We identify two configurations where the signal is dominated either by phase or amplitude changes introduced by the thermal lens. In both configurations, the light incident on the photodiodes is equal, and modes common to both arms are eliminated by differential detection. Noise suppression in this configuration is only limited by the beam pointing stability of the laser, as this affects the distribution of intensities on the two photodiodes and ultimately on the common mode rejection ratio of the amplifier. Significantly, this means that the spectrometer is shot-noise limited around the measurement frequency of 100 kHz (see Figure S2).

In the phase sensitive configuration (illustrated in Figure 2) used throughout this work, the difference ΔI between the intensities received by the two photodiodes and therefore the photothermal signal as a consequence of a phase shift, $\Delta\phi$, between the two arms induced by the thermal lens is given by

$$\Delta I = |E_1^\dagger E_1 - E_2^\dagger E_2| = \sin \Delta\phi \quad (1)$$

where E_1 and E_2 are the respective Jones vectors of the light incident on the two photodiodes. For the small phase shifts caused by the thermal lens effect, the small-angle approximation is valid and $\Delta I/I \approx \Delta\phi$ (see Supporting Information for a more complete analysis). We confirm this linear dependence by directing the excitation beam onto one arm only and observing the signal introduced by a homogeneous solution of Sunset Yellow in water as a function of laser power (Figure 1C). In further experiments using the same dye solution, we continuously vary the polarization of the excitation laser (and thus the intensity distribution) on the two arms, and we show that the thermal lens signal results exclusively from the optical path difference between the two arms (Figure 1D). To perform nanoparticle detection, we distribute the excitation beam equally on both arms, which has the advantage that any background absorbance in the solution is removed and noise

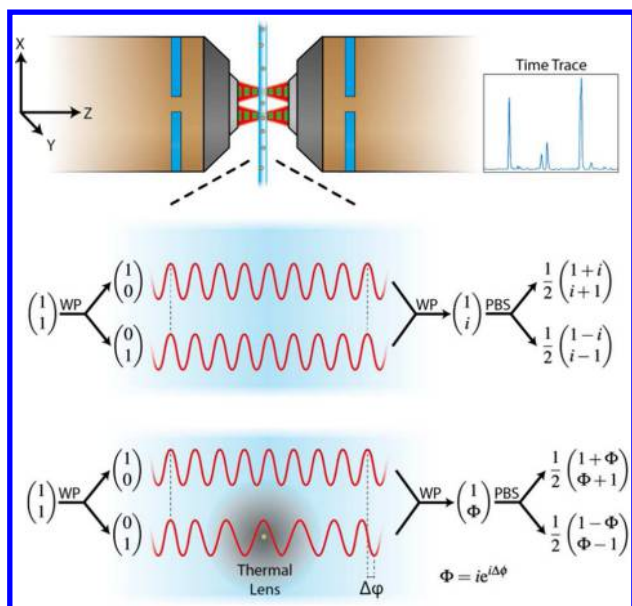


Figure 2. Illustration of the DDPI detection principle in the phase sensitive mode, showing the Jones vectors (normalized to an intensity of 2) of the probe beam as it propagates through the spectrometer. The first Wollaston prism (WP) separates the x and y components, which subsequently travel through the capillary. The second WP recombines the two components and shifts their phase by $\pi/4$ with respect to each other. A polarizing beam splitter (PBS) projects the polarization components onto separate photodiodes.

that occurs at higher concentrations from out of focus passing particles is reduced.

To test the efficacy of our detection method, we dilute stock suspensions of commercial gold nanoparticles (having diameters of 10, 20, 40, 50, 60, and 80 nm) stepwise in ethanol. A syringe pump then propels the nanoparticle solution hydrodynamically through the capillary while the lock-in amplifier records a time trace for several (<10) minutes. Because counting follows Poissonian statistics, the relative standard deviation, σ_{rel} , of the empirical concentration is equal to \sqrt{N}/N , where N is the total number of counts measured. To enable accurate concentration determination at extremely low particle concentrations, we increase the counting rate for a given concentration by maximizing the volumetric flow rate and therefore the cumulative volume that is analyzed per unit time.

The maximum flow speed at which the spectrometer can detect particles primarily depends on two factors: the measurement frequency and the response time of the lock-in amplifier (determined by its time constant). The measurement frequency should be fast enough for the thermal lens to fully develop without being distorted or displaced by the fluid flow. At a frequency of 100 kHz, this corresponds to a flow speed of approximately 0.1 m/s. Conversely, the time constant (TC) should be small enough that the photothermal signal surpasses the noise level during the transit of a particle through the probe volume. Accordingly, we expect the counting frequency to vary with flow speed up to a point where the transit time becomes too short for the particle to be detected; the threshold flow speed at which this happens depends on the time constant. Indeed, Figure 3 A illustrates a linear increase in the counting frequency when increasing the flow rate up to a threshold speed where the counting efficiency begins to drop. In the data shown, the drop-off flow speed is approximately 3 mm/s for a TC of 1 ms while it increases to 10 mm/s at a TC of 100 μ s. At

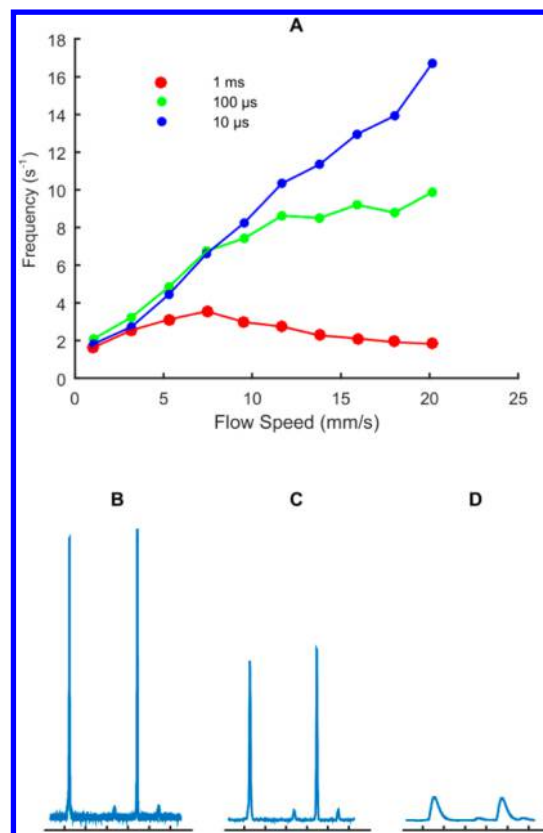


Figure 3. (A) Flow-speed dependence of the detection frequency for a 50 nm gold NP solution (at a concentration of 6 fM) measured simultaneously with TCs of 10 μ s (blue), 100 μ s (green), and 1 ms. (B,C,D) Characteristic doublet peaks observed when a 50 nm gold particle passes the two arms of the interferometer. The different signal intensities and noise levels are evident for the TCs of 1 ms (B), 100 μ s (C), and 10 μ s (D). The three plots have identical y-scales. The distance between two ticks on the x -axes is 10 ms.

a TC of 10 μ s the drop-off is not reached even at 20 mm/s. Figure 3C–E show a typical time trace of a 50 nm particle passing the two arms of the interferometer demodulated simultaneously at three different TCs and at a flow speed of 1 mm/s (yielding a residence time in the focal volume of approximately 1 ms). It is clear that the lower time constant leads to a much faster response of the lock-in amplifier but at the expense of a larger noise component present in the signal. Both arms of the interferometer are physically equivalent, and a double peak results from the fact that nanoparticles pass the arms consecutively. In this work, we do not differentiate between signals arising from either arm; however, it is possible to attribute each signal to a given arm because the arms have a phase difference of π . Additionally, at the concentrations used in the current studies, the probability of two particles passing the detection volume with a temporal separation too low to be distinguished as separate counting events is negligible. For completeness, we include a discussion of upper concentration limits in the Supporting Information.

At a flow speed of 10 mm/s, we are able to detect 10, 20, and 50 nm gold particles in the femtomolar concentration range with a TC of 100 μ s (Figure 4A–C). We extract the average number of counting events per second by measuring for several minutes and dividing the total counts by the measurement duration (see Supporting Information for the total counts and duration of each measurement). This provides a measure that is

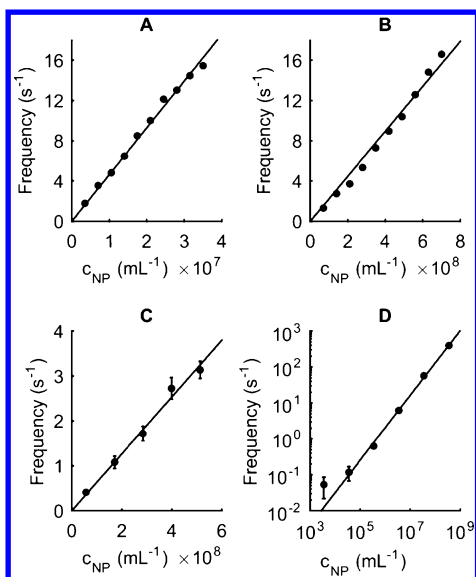


Figure 4. Concentration determination via counting for 50 (A), 20 (B), and 10 nm (C) gold nanoparticles suspended in ethanol at a flow speed of 10 mm/s. (D) Ultrahigh throughput counting of 50 nm gold at a flow speed of 100 mm/s. The error bars show the $\alpha = 0.01$ confidence interval of the true mean. Error bars are omitted when smaller than the markers.

proportional to particle concentration with excellent linearity ($r^2 > 0.99$) and accuracy, and it allows highly sensitive particle content determination in a concentration range that is not accessible by any other reported method. Interestingly and significantly, the error introduced through sample dilution is larger than the counting error, which confirms the outstanding accuracy and reproducibility of detection. To extend the concentration range to attomolar levels, we decrease the TC to 10 μ s and detect 50 nm gold particles at flow speeds of 100 mm/s, corresponding to an analyzed volume of more than 1 nL per second, which is several orders of magnitude higher than other currently available methods. Under these conditions, we can accurately determine nanoparticle content over a range of 6 orders of magnitude (Figure 4D) and at actual counting rates between 0.1 and 400 s^{-1} . Even at the lowest measurable concentration, a measurement time of 5 min is sufficient to extract high-quality data (see Supporting Information for the total counts and duration of each measurement). From the counting data, we are able to calculate effective volumes that particles must pass through to be detected. The size of the effective detection volume depends on the flow velocity, the time constant of the lock-in-amplifier and the size of the nanocrystal. For experiments performed at flow speeds of 10 mm/s, we obtain effective detection volumes of 0.5 fL for 10 nm particles, 3.3 fL for 20 nm particles, and 312 fL for 50 nm particles. For the experiment using a flow speed of 100 mm/s, we estimate an effective detection volume of 58 fL. The fraction of all particles moving through the capillary which are detected is 4×10^{-5} for 10 nm particles, 1×10^{-5} for 20 nm particles, and 3×10^{-3} for 50 nm particles (all at a flow speed of 10 mm/s). From these values, we estimate that a capillary diameter of 600 nm would be required for quantitative detection of 10 nm particles and 5 μ m for 50 nm particles.

An important parameter needed in many chemical and biological applications is the mean size of a particle population. As demonstrated in Figure 1 C, the photothermal signal is

directly proportional to the absorbed energy and therefore to the absorbance cross section.³³ This makes our spectrometer an ideal tool in nanoparticle sizing applications. The interaction of light (of wavelength λ) with a particle of radius, r , in a medium with refractive index, N_2 , is governed by the size parameter, $x = 2\pi N_2 r \lambda^{-1}$. For particles with small size parameter ($x \ll 1$) the absorbance cross section can be expressed in the electrostatic approximation as

$$C_{\text{abs}} = 4\pi r^2 x \cdot \text{Im} \left\{ \frac{\epsilon_1 - \epsilon_2}{\epsilon_1 + 2\epsilon_2} \right\} \quad (2)$$

with complex permittivities of particle ϵ_1 and medium ϵ_2 . For spherical gold particles in ethanol, this approximation is valid up to a radius of 60 nm, after which the size dependence must be considered using Mie theory.¹⁶ Figure 5 shows both the

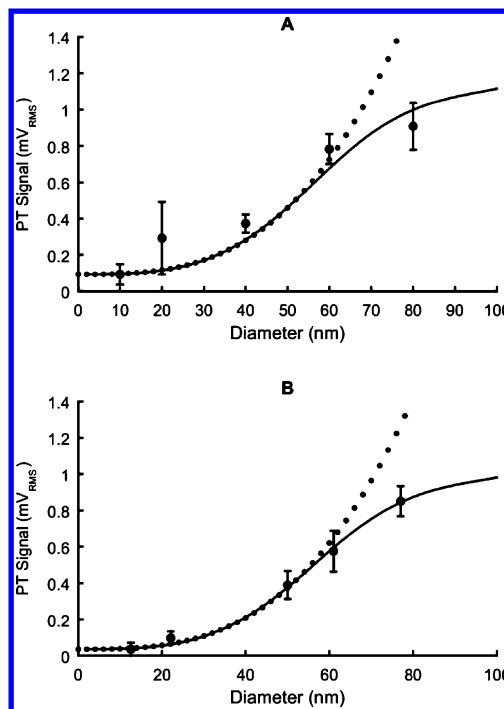


Figure 5. Photothermal signal as a function of size for commercially sourced particles (A) and particles prepared via seed-mediated growth (B). The dotted lines show the trend predicted by the electrostatic approximation, and the solid lines show the full Mie calculation. The size of the error bars is equal to one standard deviation.

electrostatic approximation and full Mie calculation together with the size dependence of the photothermal signal for commercially sourced nanoparticles and nanoparticles synthesized via seed-mediated growth. In the current studies, we do not control the trajectory of the nanoparticles through the detection volume, which makes it impossible to assign a size to an individual signal. For example, a large particle passing the excitation beam out of focus can result in a similar photothermal signal as a small particle passing precisely through the focal volume. However, we are still able to extract meaningful size information for particle ensembles via signal statistics. To obtain the data shown in Figure 5, we simply divide the time traces into discrete time packages of 20 s, and we select the maximum signal of each package. Importantly, the mean of the obtained maxima is in excellent agreement with theory. We believe that better agreement in the case of freshly

prepared particles originates from the presence of aggregates in the commercial sample, especially in the case of small particles with average diameters of 10 and 20 nm.

In conclusion, we have presented DDPI, a method that is capable of rapidly and accurately quantifying gold nanoparticle populations at extremely low concentrations and extracting size information. This method significantly improves the sensitivity of gold-nanoparticle-based assays and enables a wealth of potential applications ranging from process control to environmental monitoring. While variation of other experimental parameters will undoubtedly be useful in improving the signal-to-noise ratio (such as larger excitation and probe intensities, high NA objectives, and different solvents³⁴), our detection scheme provides the maximum possible signal-to-noise ratio for a given configuration as it is shot-noise limited and recovers both polarization components of the signal. The high flow rates and the simple interface with microfluidic systems make it readily integrable as a detection method into a wide variety of analytical platforms. As a next step, we aim to better confine the stream of particles through the detection volume (e.g., using a nanochannel) to increase the detection efficiencies and allow the direct measurement of the absorbance cross section of each individual particle. Such refinements will allow the extraction of size distribution data for particle populations.

METHODS

Colloidal solutions of 10, 20, 40, 60, and 80 nm diameter gold nanoparticles (BBI Solutions), 50 nm gold nanoparticles (Sigma-Aldrich), and Sunset Yellow FCF (90%, Sigma-Aldrich) were used as received. Ethanol ($\geq 99.9\%$, Uvasol) was purchased from Merck Millipore. The seed-mediated growth of gold nanoparticles was carried out via established literature methods.³⁵ A 200 μm inner diameter and 360 μm outer diameter fused silica capillary was obtained from Polymicro Technologies. A section of the polyimide coating on the capillary was removed using hot sulfuric acid to ensure transparency to the laser light. Aliquots from the gold nanoparticle stock solutions were diluted in ethanol to the desired concentrations prior to use. Sunset Yellow was dissolved in deionized water to a final concentration of 100 $\mu\text{mol/L}$.

For DDPI measurements a 632 nm HeNe laser (21.5 mW, ThorLabs) and a 532 nm OPSL laser (120 mW, Coherent Obis LS) are separated using a silica Wollaston prism (1° separation angle, Bernhard Halle Nachfl. GmbH) and coupled via a 4f-system into a microscope objective (40 \times , 0.75 NA, Nikon Plan Fluor) which focuses the beams into the center of the fused silica capillary. After the capillary, the beams are collected and recombined using an identical objective, 4f-system and Wollaston prism. The 532 nm beam is removed by a filter and the probe beam passes a $\lambda/2$ plate before its polarization components are projected on two silicon photodiodes (FDS1100, Thorlabs). The diodes are amplified by a transimpedance amplifier (HF2TA, Zurich Instruments) and connected to the differential input of a lock-in amplifier (HF2LI, Zurich Instruments). The lock-in amplifier also serves as a function generator to modulate the pump-laser at 100 kHz.

ASSOCIATED CONTENT

Supporting Information

The Supporting Information is available free of charge on the ACS Publications website at DOI: 10.1021/acs.analchem.6b04540.

Theoretical description of the interferometer; shot noise limited detection; transmission electron micrographs of the gold nanoparticles; detailed schematic of the optical setup (PDF)

AUTHOR INFORMATION

Corresponding Author

*E-mail: Andrew.deMello@chem.ethz.ch.

ORCID

David Müller: 0000-0003-1914-3768

Andrew deMello: 0000-0003-1943-1356

Notes

The authors declare no competing financial interest.

ACKNOWLEDGMENTS

We thank Olga Nazarenko for taking transmission electron micrographs and Stavros Stavrakis for helpful discussions.

REFERENCES

- (1) Zhou, W.; Gao, X.; Liu, D. B.; Chen, X. Y. *Chem. Rev.* **2015**, *115*, 10575–10636.
- (2) Saha, K.; Agasti, S. S.; Kim, C.; Li, X. N.; Rotello, V. M. *Chem. Rev.* **2012**, *112*, 2739–2779.
- (3) Abadeer, N. S.; Murphy, C. J. *J. Phys. Chem. C* **2016**, *120*, 4691–4716.
- (4) Raschke, G.; Kowarik, S.; Franzl, T.; Sonnichsen, C.; Klar, T. A.; Feldmann, J.; Nichtl, A.; Kurzinger, K. *Nano Lett.* **2003**, *3*, 935–938.
- (5) Zijlstra, P.; Paulo, P. M.; Orrit, M. *Nat. Nanotechnol.* **2012**, *7* (6), 379–82.
- (6) Crut, A.; Maioli, P.; Del Fatti, N.; Vallee, F. *Chem. Soc. Rev.* **2014**, *43*, 3921–3956.
- (7) Ignatovich, F. V.; Novotny, L. *Phys. Rev. Lett.* **2006**, *96*, 013901.
- (8) Jacobsen, V.; Stoller, P.; Brunner, C.; Vogel, V.; Sandoghdar, V. *Opt. Express* **2006**, *14*, 405–414.
- (9) Faez, S.; Lahini, Y.; Weidlich, S.; Garmann, R. F.; Wondraczek, K.; Zeisberger, M.; Schmidt, M. A.; Orrit, M.; Manoharan, V. N. *ACS Nano* **2015**, *9*, 12349–12357.
- (10) Nedosekin, D. A.; Sarimollaoglu, M.; Galanzha, E. I.; Sawant, R.; Torchilin, V. P.; Verkhusha, V. V.; Ma, J.; Frank, M. H.; Biris, A. S.; Zharov, V. P. *J. Biophotonics* **2013**, *6*, 425–434.
- (11) Zhu, S.; Ma, L.; Wang, S.; Chen, C.; Zhang, W.; Yang, L.; Hang, W.; Nolan, J. P.; Wu, L.; Yan, X. *ACS Nano* **2014**, *8*, 10998–1006.
- (12) Liang, L.; Zuo, Y. F.; Wu, W.; Zhu, X. Q.; Yang, Y. *Lab Chip* **2016**, *16*, 3007–3014.
- (13) Yang, H.; Cornaglia, M.; Gijs, M. A. M. *Nano Lett.* **2015**, *15*, 1730–1735.
- (14) Kuyper, C. L.; Budzinski, K. L.; Lorenz, R. M.; Chiu, D. T. *J. Am. Chem. Soc.* **2006**, *128*, 730–731.
- (15) Kuyper, C. L.; Fujimoto, B. S.; Zhao, Y.; Schiro, P. G.; Chiu, D. T. *J. Phys. Chem. B* **2006**, *110*, 24433–24441.
- (16) Bohren, C. F.; Huffman, D. R. *Absorption and Scattering of Light by Small Particles*; Wiley-VCH Verlag GmbH & Co. KGaA: Weinheim, 1998.
- (17) Berciaud, S.; Cognet, L.; Blab, G. A.; Lounis, B. *Phys. Rev. Lett.* **2004**, *93*, 257402.
- (18) Skala, M. C.; Crow, M. J.; Wax, A.; Izatt, J. A. *Nano Lett.* **2008**, *8*, 3461–3467.
- (19) Lasne, D.; Blab, G. A.; Berciaud, S.; Heine, M.; Groc, L.; Choquet, D.; Cognet, L.; Lounis, B. *Biophys. J.* **2006**, *91*, 4598–604.
- (20) Shimizu, H.; Mawatari, K.; Kitamori, T. *Anal. Chem.* **2009**, *81*, 9802–9806.
- (21) Yamaoka, S.; Kataoka, Y.; Kazama, Y.; Fujii, Y.; Hibara, A. *Sens. Actuators, B* **2016**, *228*, 581–586.
- (22) Seta, N.; Mawatari, K.; Kitamori, T. *Anal. Sci.* **2009**, *25*, 275–278.

- (23) Kulzer, F.; Laurens, N.; Besser, J.; Schmidt, T.; Orrit, M.; Spaink, H. P. *ChemPhysChem* **2008**, *9*, 1761–1766.
- (24) Maceiczky, R. M.; deMello, A. J. *J. Phys. Chem. C* **2014**, *118*, 20026–20033.
- (25) Lignos, I.; Stavrakis, S.; Kilaj, A.; deMello, A. J. *Small* **2015**, *11*, 4009–4017.
- (26) Phillips, T. W.; Lignos, I. G.; Maceiczky, R. M.; deMello, A. J.; deMello, J. C. *Lab Chip* **2014**, *14*, 3172–3180.
- (27) Maceiczky, R. M.; Lignos, I. G.; deMello, A. J. *Curr. Opin. Chem. Eng.* **2015**, *8*, 29–35.
- (28) Lignos, I.; Stavrakis, S.; Nedelcu, G.; Protesescu, L.; Demello, A. J.; Kovalenko, M. V. *Nano Lett.* **2016**, *16*, 1869–1877.
- (29) Selmke, M.; Heber, A.; Braun, M.; Cichos, F. *Appl. Phys. Lett.* **2014**, *105*, 013511.
- (30) Boyer, D.; Tamarat, P.; Maali, A.; Lounis, B.; Orrit, M. *Science* **2002**, *297*, 1160–1163.
- (31) Cassano, C. L.; Mawatari, K.; Kitamori, T.; Fan, Z. H. *Electrophoresis* **2014**, *35*, 2279–91.
- (32) Cognet, L.; Berciaud, S.; Lasne, D.; Lounis, B. *Anal. Chem.* **2008**, *80*, 2288–2294.
- (33) Selmke, M.; Braun, M.; Cichos, F. *J. Opt. Soc. Am. A* **2012**, *29*, 2237–2241.
- (34) Gaiduk, A.; Ruijgrok, P. V.; Yorulmaz, M.; Orrit, M. *Chemical Science* **2010**, *1*, 343–350.
- (35) Niu, J.; Zhu, T.; Liu, Z. *Nanotechnology* **2007**, *18*, 325607.